Nuclear Inst. and Methods in Physics Research, A 1002 (2021) 165251

Contents lists available at ScienceDirect

Nuclear Inst. and Methods in Physics Research, A

journal homepage: www.elsevier.com/locate/nima

Atomic scale Monte-Carlo simulations of neutron diffraction experiments on stoichiometric uranium dioxide up to 1664 K

S. Xu [a], G. Noguere [a,*], L. Desgranges [a], J.I. Marquez Damian [b]

[a] CEA, DES, IRESNE, Cadarache, F-13108 Saint Paul les Durance, France
[b] Neutron Physics Departement and Instituto Balseiro, Centro Atomico Bariloche, CNEA, Argentina

ARTICLE INFO

Keywords:
Neutron diffraction
Uranium dioxide
Phonon density of states
Monte-Carlo simulation

ABSTRACT

The neutron transport in nuclear fuels depends on the crystalline structure of materials when neutron energies lie below a few eV. For that purpose, the theoretical formalism that describes the neutron elastic and inelastic scatterings by crystals has been implemented in the CINEL processing tool in order to provide temperature-dependent neutron cross sections usable by the Monte-Carlo code TRIPOLI4®. The performances of the Monte-Carlo calculations are illustrated with the analysis of neutron powder diffraction data on UO_2 measured up to 1664 K with the D4 and D20 diffractometers of the Institute Laue–Langevin (Grenoble, France). The comparison of the experimental and simulated pair distribution functions confirms the unusual decrease of the U–O atomic distances with increasing temperature when an ideal fluorite structure ($Fm\bar{3}m$ space group) with harmonic atomic vibrations is assumed over the full temperature range. The flexibility of the CINEL code allowed to explore disorder or anharmonic oxygen vibrations in the $Fm\bar{3}m$ space group by using either a four-site model with a relaxation term or a structure factor equation with a non-zero anharmonic third-cumulant coefficient. As none of these models succeeded to improve the agreement with the experiments, recent works that propose other local crystalline symmetries for UO_2 at elevated temperatures were investigated with the CINEL code. The case of the $Pa\bar{3}$ symmetry is briefly discussed in this paper.

1. Introduction

Low-energy neutrons (below a few eV) have been used since the sixties [1,2] to probe the crystalline structure of uranium dioxide (UO_2) from room temperature to normal nuclear reactors operating conditions. Despite these experimental and theoretical efforts, crystalline structure effects are not yet routinely taken into account in industrial neutronic simulation schemes of nuclear power reactors. Temperature effects are often calculated via a simple Free Gas Model. Therefore, validating the crystalline effects at the microscopic level is still a necessity to motivate an update of the neutron scattering treatment in neutronic simulation schemes.

The aim of the paper is to show the performances of modern Monte-Carlo neutron transport codes for revisiting the analysis of neutron diffraction experiments measured at elevated temperatures, which were originally designed to study the temperature effects on the UO_2 lattice arrangement. Indeed, if the fluorite structure ($Fm\bar{3}m$ space group) of UO_2 is well established at room temperature, the understanding of the unusual relaxation with the increasing temperature of the oxygen atoms from their regular positions is still under discussion. Among the few neutron diffraction measurements on stoichiometric uranium dioxide reported in the literature, we have selected the works of Ruello [3] and Ma [4], whose data are still available at the Institute Laue–Langevin (ILL) of Grenoble (France). The experiments were performed on the D20 and D4 diffractometers, respectively. They consisted in measuring the temperature-dependent neutron scattering yield $Y^T_{\text{exp}}(\theta)$ as a function of the scattering angle θ. The two data sets cover a wide temperature range from room temperature to 1664 K. The originality of our work relies on the use of the Monte-Carlo code TRIPOLI4® [5] to simulate the experimental diffraction patterns by taking into account the multiple neutron scattering effects and the multiphonon contribution. The experimental corrections, which are not introduced in the Monte-Carlo simulations, are the background correction, the angular offset and the angular response function of the diffractometer. They are deduced from the data by applying a Rietveld-type structure refinement [6] on the neutron scattering yields simulated with the TRIPOLI4® code. Final results mainly depend on the neutron scattering cross sections of uranium and oxygen in UO_2 which were introduced in the simulations.

The low-energy neutron cross section formalism is well documented [7]. The theory was implemented in dedicated processing codes, such as NJOY [8] and FLASSH [9]. They provide neutron application libraries for Monte-Carlo and deterministic neutron transport codes [10,11].

---

[*] Corresponding author.
E-mail address: gilles.noguere@cea.fr (G. Noguere).

https://doi.org/10.1016/j.nima.2021.165251
Received 31 August 2020; Received in revised form 8 March 2021; Accepted 14 March 2021

For demonstrating the performances of the TRIPOLI4® code, we have developed a Python code, namely CINEL, which can be virtually applied on various solids, liquids and gases of interest for the nuclear industry. A few solid materials (graphite, niobium and beryllium) and liquid (H_2O) were already studied. For solid materials, CINEL encompasses the theory needed to calculate effects of the neutron Bragg edges diffraction and dynamics structure factors $S_j(Q,\omega)$ of each atom j in the crystal as a function of the momentum transfer $\hbar Q$ and energy transfer $\varepsilon = \hbar\omega$. The present paper only focuses on the neutron induced inelastic and coherent-elastic scattering reactions on UO_2. The incoherent-elastic scattering is neglected because of its weak contribution to the scattering process, as indicated in the neutron scattering length and cross section tables [12].

The main expressions involved in the low-energy neutron scattering formalism are reported in Section 2. The Section 3 briefly describes the measurements performed at ILL and the calculation scheme. The interpretation of the data with the Monte-Carlo neutron transport code TRIPOLI4® is presented in Section 4. Extensions of the CINEL model to account for anharmonic oxygen vibrations in the $Fm\bar{3}m$ space group or other crystalline symmetries for UO_2 at elevated temperatures are discussed in Section 5.

2. Low-energy neutron cross section formalism

2.1. Total neutron cross section

The TRIPOLI4® code is used to simulate the neutron transport in the UO_2 sample, for which the total neutron cross section is a key quantity for computing the distance traveled by the neutron between two interactions. The total neutron cross sections of uranium ($U \equiv {}^{238}U$) and oxygen ($O \equiv {}^{16}O$) in UO_2 as a function of the incident neutron energy E are the sum of the partial neutron cross sections:

$$\sigma_{t_U}(E) = \sigma_{\gamma_U}(E) + \sigma_{f_U}(E) + \sigma_{n_U}(E), \tag{1}$$

$$\sigma_{t_O}(E) = \sigma_{\gamma_O}(E) + \sigma_{n_O}(E), \tag{2}$$

where the indexes γ, f and n are related to the radiative capture, fission and scattering reactions, respectively. In the neutronic simulations of nuclear power reactors, the neutron induced capture, fission and elastic reactions on uranium and oxygen are routinely calculated in the framework of the R-Matrix theory [13] and Doppler broadened at a given temperature T with a Free Gas Model, whose validity of the formalism is discussed in Ref. [14]. However, for E lower than a few eV, the neutron scattering cross section has to be divided in an elastic and inelastic parts, with coherent and incoherent terms. In the case of neutron induced scattering reactions on UO_2, the incoherent elastic cross section is negligible and the neutron scattering cross section reduces to:

$$\sigma_{n_j}(E) = \sigma^{\mathrm{el}}_{\mathrm{coh}}(E) + \sigma^{\mathrm{inel}}_j(E) \tag{3}$$

where j represents the uranium or oxygen atoms in UO_2. The first term in Eq. (3) is the coherent elastic scattering cross section which accounts for the crystalline structure of UO_2. The second term is the inelastic scattering cross section that depends on the dynamical properties of each atom j in the crystal.

The components of the neutron scattering process are shown in Fig. 1 as a function of E for $T = 300$ K. The principles of the calculations implemented in the CINEL code are presented in Sections 2.2 and 2.3. The comparison with the neutron elastic scattering cross sections calculated with a Free Gas Model approximation highlights the large differences between the formalism, which may introduce biases in neutronic calculations. For example, the use of the Free Gas Model can imply a bias of about 100 pcm (0.1%) on the neutron multiplication factor k_{eff} calculated for integral benchmarks with UOX fuel. Such a bias cannot be seen as a negligible source of uncertainties, given that the total uncertainty on the calculated k_{eff} should be lower than 500 pcm (0.5%).

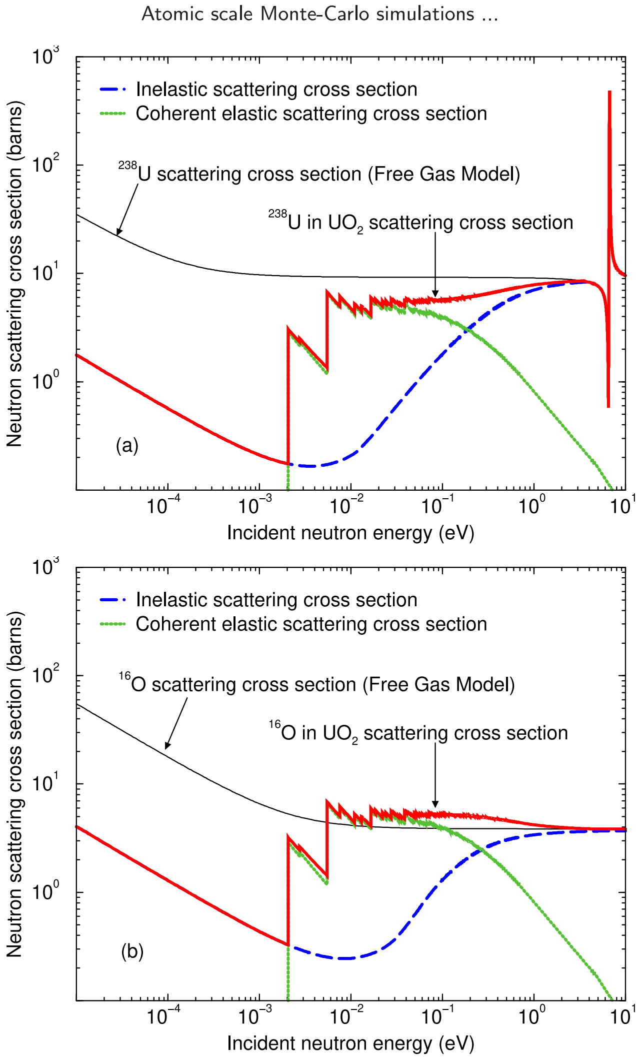

Fig. 1. Neutron scattering cross sections of ${}^{238}U$ in UO_2 (a) and ${}^{16}O$ in UO_2 (b) as a function of the incident neutron energy at $T = 300$ K. The inelastic and coherent elastic scattering cross sections were calculated with the CINEL code by using equations presented in Sections 2.2 and 2.3. The neutron cross sections calculated with the Free Gas Model are plotted for comparison. The structure observed at 6.6 eV corresponds to the first s-wave ${}^{238}U$ resonance.

2.2. Double-differential inelastic scattering cross section

In the low neutron energy range, the slowing down of neutrons in UO_2 depends on the energy and angular distribution of the inelastic scattering process. The mathematical expression of the corresponding double-differential inelastic neutron scattering cross section is well described in the literature. The main equations are summarized in Ref. [8]. They were obtained in the framework of the incoherent scattering approximation that allows to neglect the interference terms in the case of polycrystalline materials and to express the double-differential neutron scattering cross section of each atom j separately as follows [16]:

$$\frac{d^2\sigma^{\mathrm{inel}}_j(E)}{dE'd\theta} = \frac{\sigma_j}{4\pi\hbar}\sqrt{\frac{E'}{E}}\, S_j(Q,\omega), \tag{4}$$

where E' stands for the energy of the scattered neutron, σ_j is the bound neutron elastic scattering cross section and $S_j(Q,\omega)$ is the dynamic structure factor [17] which is defined as a function of the momentum transfer $\hbar Q$ and energy transfer $\varepsilon = \hbar\omega$. A suitable analytical expression

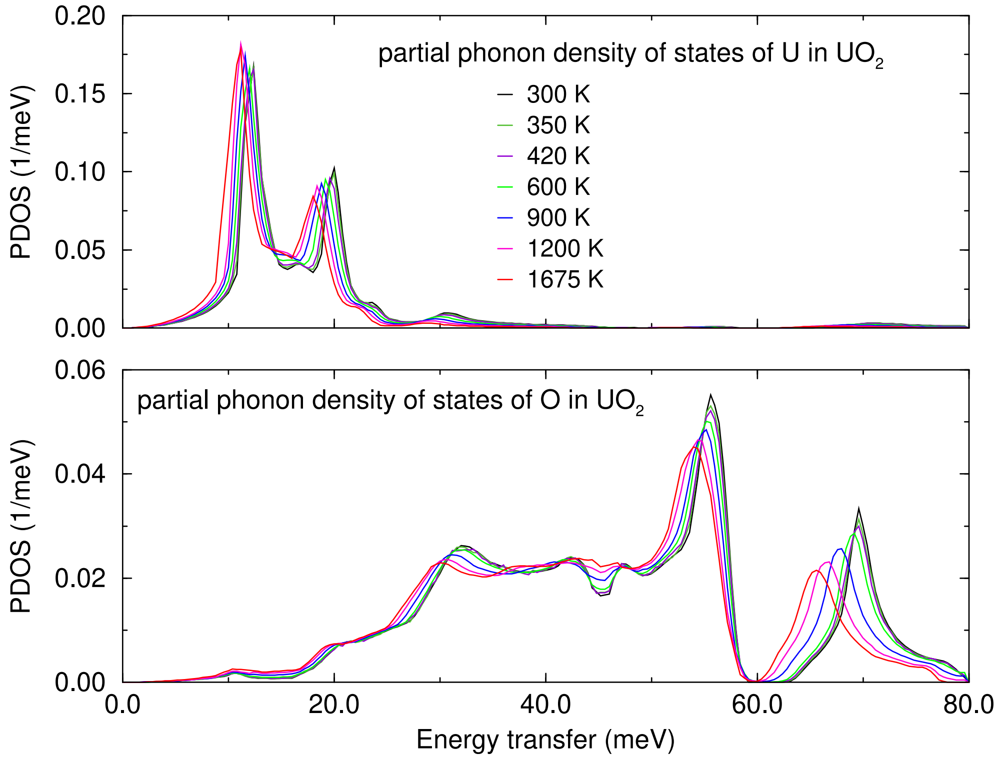

Fig. 2. Temperature-dependent partial phonon density of states of uranium and oxygen in UO$_2$ as a function of the energy transfer ε [15].

was obtained in the framework of the incoherent Gaussian approximation [18] thanks to the conventionally called phonon expansion method [19]:

$$S_j(Q,\omega) = \mathrm{e}^{-\frac{\hbar^2 Q^2}{2M_j k_B T}\Lambda_j} \sum_{n=1}^{\infty} \frac{1}{n!}\left(\frac{\hbar^2 Q^2}{2M_j k_B T}\Lambda_j(T)\right)^n \mathcal{T}_n(\omega), \tag{5}$$

where k_B is the Boltzmann constant, n represents the phonon expansion order, M_j is the mass of the nucleus j, $\Lambda_j(T)$ stands for the temperature-dependent Debye–Waller coefficient and $\mathcal{T}_n(\omega)$ has the generic form:

$$\mathcal{T}_n(\omega) = \int_{-\infty}^{\infty} \mathcal{T}_1(\omega')\mathcal{T}_{n-1}(\omega-\omega')d\omega'. \tag{6}$$

The one-phonon term is given by:

$$\mathcal{T}_1(\omega) = \frac{1}{\Lambda_j(T)} P_j(\omega). \tag{7}$$

This term explicitly depends on the Debye–Waller coefficient:

$$\Lambda_j(T) = \int_{-\infty}^{\infty} P_j(\omega)\mathrm{d}\omega, \tag{8}$$

for which an analytical expression of $P_j(\omega)$ has been derived under the cubic symmetry:

$$P_j(\omega) = \rho_j(\omega)\mathrm{e}^{\frac{\hbar\omega}{2k_B T}}\left(\frac{2\hbar\omega}{k_B T}\sinh\left(\frac{\hbar\omega}{2k_B T}\right)\right)^{-1}, \tag{9}$$

with

$$\int_0^{\infty} \rho_j(\omega)d\omega = 1. \tag{10}$$

The partial phonon density of states $\rho_j(\omega)$ is the main physical quantity involved in the theoretical description of the double-differential inelastic scattering cross section. Results obtained from the analysis of inelastic scattering measurements performed at ILL [15] are shown in Fig. 2. The five normal modes of vibration of UO$_2$ can be distinguished around 10 meV, 20 meV, 30 meV, 55 meV and 70 meV. The two first peaks correspond to the translational and longitudinal acoustic phonon modes of the uranium atoms. The highest energy structures are dominated by the optical phonon modes of the oxygen atoms.

The inelastic scattering cross sections of O and U in UO$_2$ calculated at $T = 300$ K with the CINEL code are shown in Fig. 1. It is the dominant scattering process for cold and hot neutrons.

2.3. Coherent elastic scattering cross section

The formalism of the coherent elastic scattering cross section is well documented in Ref. [22]. This section presents the main equations established for harmonic atomic vibrations.

Any crystal can be characterized by a periodic unit cell containing N atoms. In the direct lattice, it is defined by a set of unit vectors $\vec{a}$, $\vec{b}$, $\vec{c}$ of lengths a, b, c and volume $V_{uc} = \vec{a}\cdot(\vec{b}\times\vec{c})$. The angles between them are conventionally denoted α, β and γ. The position of the jth atom located at the point (x_j, y_j, z_j) is given by:

$$\vec{p}_j = x_j\vec{a} + y_j\vec{b} + z_j\vec{c} \quad x_j,\ y_j,\ z_j \in [0,1]. \tag{11}$$

In the reciprocal lattice, the unit vectors become:

$$\vec{\tau}_a = \frac{2\pi}{V_{uc}}(\vec{b}\times\vec{c}), \quad \vec{\tau}_b = \frac{2\pi}{V_{uc}}(\vec{c}\times\vec{a}), \quad \vec{\tau}_c = \frac{2\pi}{V_{uc}}(\vec{a}\times\vec{b}), \tag{12}$$

and indices h, k, l denote planes (hkl) orthogonal to the reciprocal lattice vector:

$$\vec{\tau}_{hkl} = h\vec{\tau}_a + k\vec{\tau}_b + l\vec{\tau}_c. \tag{13}$$

The neutron diffraction will occur from the planes (hkl) that are oriented at the correct angle to fulfill the Bragg condition. The coherent elastic cross section per atom emerges from the sum of all the neutron scattering contributions over the N atoms of the unit cell and plans (hkl). The analytical expression for crystal powder with randomly distributed grains is given by:

$$\sigma_{\mathrm{coh}}^{\mathrm{el}}(E) = \frac{\pi^2\hbar^2}{mNV_{uc}E} \sum_{hkl}^{E\geq E_{hkl}} d_{hkl}\left|F(\vec{\tau}_{hkl})\right|^2, \tag{14}$$

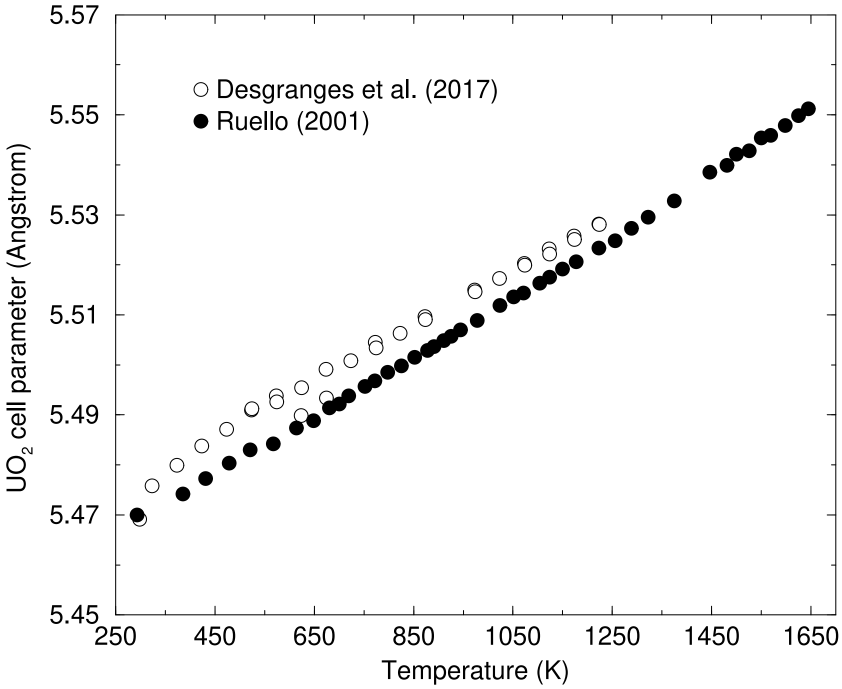

Fig. 3. Temperature-dependent cell parameters for UO_2 obtained by Ruello [20] and Desgranges [21] from the Rietveld refinement of neutron diffraction patterns measured on the D20 and D4 diffractometers, respectively.

Table 1
Atom site occupancy in UO_2 unit cell with $Fm\bar{3}m$ symmetry [23].

Atom	j	x	y	z
U	1	0	0	0
U	2	0	1/2	1/2
U	3	1/2	0	1/2
U	4	1/2	1/2	0
O	5	1/4	3/4	3/4
O	6	1/4	1/4	3/4
O	7	1/4	1/4	1/4
O	8	1/4	3/4	1/4
O	9	3/4	3/4	1/4
O	10	3/4	1/4	1/4
O	11	3/4	1/4	3/4
O	12	3/4	3/4	3/4

with

$$F(\vec{\tau}_{hkl}) = \sum_{j=1}^{N} b_j \exp\left(-\frac{\hbar^2 \tau_{hkl}^2}{4 M_j k_B T} \Lambda_j(T)\right) e^{i\vec{\tau}_{hkl}\cdot\vec{\rho}_j}, \qquad (15)$$

in which m is the neutron mass, $E_{hkl} = \hbar^2\tau_{hkl}^2/(8m)$ represents the Bragg edges, $d_{hkl} = 2\pi/\tau_{hkl}$ stands for the distance between adjacent planes (hkl) and b_j is the coherent bound scattering length. In this work, the summation over the indexes h, k and l runs until reaching the condition $d_{hkl} < 0.1$ Å.

Eq. (14) will be applied to UO_2 assuming a $Fm\bar{3}m$ symmetry with harmonic atomic vibrations over the full temperature range of interest for this work. The UO_2 unit cell contains $N = 12$ atoms, with 4 atoms of uranium and 8 atoms of oxygen. The cubic symmetry leads to cell parameters $a = b = c$ and angles $\alpha = \beta = \gamma = 90°$. The positions of the uranium and oxygen atoms are reported in Table 1. Fig. 3 shows the two sets of temperature-dependent cell parameters [20,21] which were used to simulate the neutron diffraction patterns measured at ILL. The observed differences are discussed in Section 4.

The coherent elastic scattering cross section calculated at $T = 300$ K with the CINEL code is shown in Fig. 1. It is the dominant scattering process for thermal neutrons with energies close to 25.3 meV.

3. Neutron diffraction studies of UO_2

3.1. Experimental programs

The performances of the TRIPOLI4® code are illustrated with two sets of data measured at ILL on the D4 and D20 diffractometers. The description of the experiments and the results are reported in Refs [3,21]. The detailed characteristics of each instrument can be found elsewhere [24,25]

The left hand side of Fig. 4 shows schematic top views of the D4 and D20 spectrometers. The right hand drawings represent the simplified geometries introduced in the Monte-Carlo code TRIPOLI4®. From the point of view of the neutron transport physics, both spectrometers share the same basic design. The experimental technique consists in measuring the neutron scattering yield $Y_{\mathrm{exp}}^{T}(\theta)$ as a function of the scattering angle θ and temperature T.

For D4, the distance between the sample and the ^3He detectors is 1.146 m. The detector array covers scattering angles ranging from 1.5° to 140° with an angular resolution of 0.125°. The monoenergetic neutron beam of 331.18 meV (0.4970 Å) emerges from a Cu (220) monochromator and passes through filters, which were designed to remove the second harmonic contaminations. The neutron beam was focused to the sample, which was mounted in a furnace placed at the center of the spectrometer. The sample consisted in a stack of two UO_2 pellets of 8.3 mm in diameter and 14 mm in height sealed under vacuum in a quartz tube. The density of the pellets is 10.76 g/cm^3 which corresponds to 98.2% of the theoretical density. The measurements were performed with temperatures ranging from 298 K to 1273 K.

For D20, the ^3He detector ring is located at 1.471 m from the sample. It covers scattering angles ranging from 0° to 156.3° with an angular resolution of 0.1°. The energy of the incident neutrons, coming from a Cu (200) monochromator, was equal to 48.05 meV (1.3048 Å). The higher order harmonic contaminations are not suppressed. Their contributions in the incident neutron beam are about 0.3%. Two UO_2 pellets (with a diameter of 8 mm and a height of 10 mm) were placed in a niobium tube on the bottom of a niobium furnace, allowing to investigate a wide temperature range from 292 K to 1664 K.

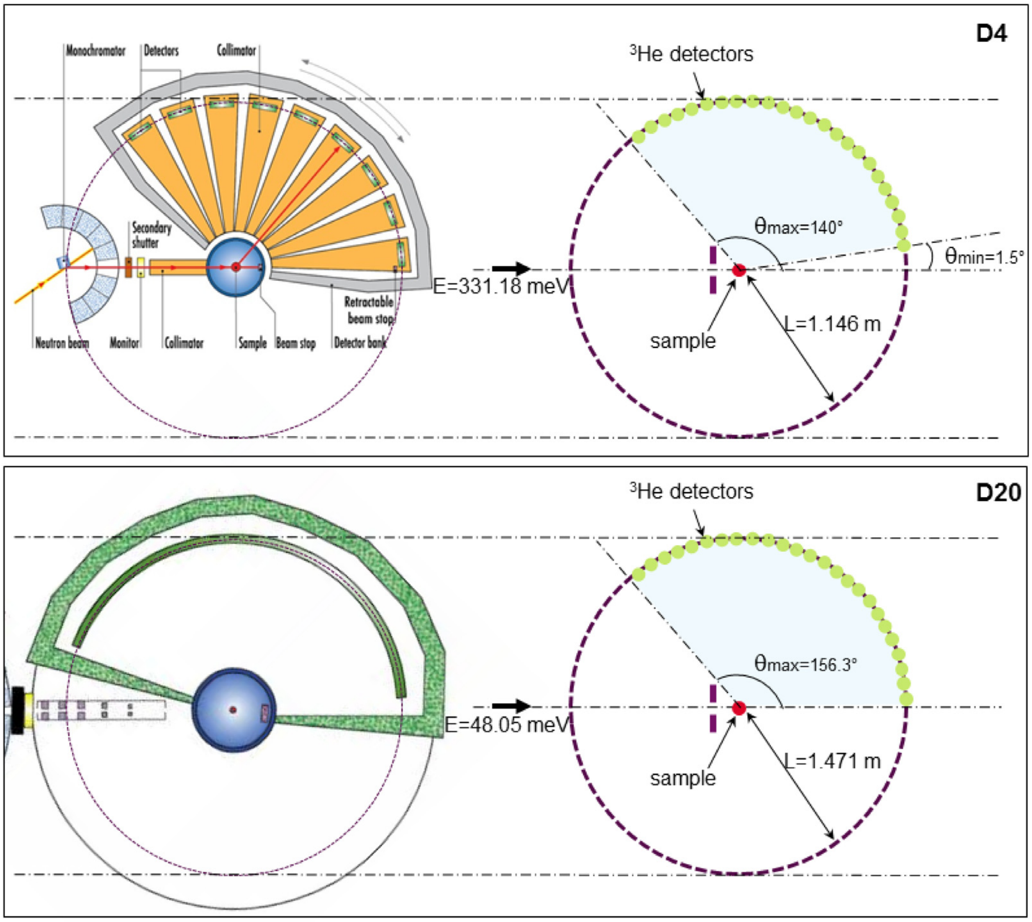

Fig. 4. The left hand drawings represent simplified top view of the D4 and D20 diffractometers of the Institute Laue–Langevin. Those on the right hand side show the geometries introduced in the Monte-Carlo calculations.

The experiments consisted in a sequence of UO_2 and empty-sample measurements. The data reduction steps were handled with ILL in-house codes, whose major issues could come from the background subtraction. The background is mainly due to neutrons scattered by the sample-holder and its environment. It is removed by subtracting the neutron scattering yield measured during the empty-sample sequence times an empirical determined effective sample transmission factor. In the present work, the background subtraction was only revisited in the case of the Ruello's data measured on D20. Fig. 5 shows neutron diffraction patterns at $T = 292$ K, in which many structures due to the large amount of niobium can be observed. Most of them were removed by using an effective transmission factor of 0.87.

3.2. Calculation scheme

The calculation scheme used in this work are summarized in Fig. 6. The first step consists in producing with the CINEL processing tool an application library that contains temperature-dependent neutron scattering cross sections. CINEL has been developed in Python in order to take full advantages of the latest CPU and GPU accelerated libraries. The neutron scattering cross sections are stored in ascii files by following the ENDF-6 format requirements for thermal scattering laws [26]. The second step consists in simulating the neutron diffraction experiments with the Monte-Carlo code TRIPOLI4®. The high performance computing capabilities allow to reach a relative statistical uncertainty of about $\pm 0.5\%$ on the top of the Bragg peaks (and $\pm 5.0\%$ in between) in a few minutes for a given temperature. The last step is devoted to account for experimental corrections not introduced in the Monte-Carlo simulations. The theoretical neutron yield Y_{th}^T as a function of the scattering angle θ is calculated from the neutron yields Y_{T4}^T provided by TRIPOLI4® as follows:

$$Y_{th}^T(\theta) = \int_0^{2\pi} R_\theta(\theta') Y_{T4}^T(\theta' + \Delta\theta) \mathrm{d}\theta' + C_{\mathrm{bkg}}, \tag{16}$$

in which C_{bkg} represents a constant background, $\Delta\theta$ accounts for a non-zero angular offset and $R_\theta(\theta')$ stands for the angular response function of the diffractometer. The angular offset is given by [27]:

$$\Delta\theta = C + \frac{x\sin(\theta) - y\cos(\theta)}{L} \tag{17}$$

where C is a constant angular shift and (x, y) accounts for the sample displacement from the center of the diffractometer of radius L. In this work, the angular response function of the instrument is approximated by a Gaussian, whose Full Width at Half Maximum is given by the Caglioti expression [28]:

$$\mathrm{FWHM}^2(\theta) = U_1 \tan^2\left(\frac{\theta}{2}\right) + U_2 \tan\left(\frac{\theta}{2}\right) + U_3 \tag{18}$$

Fig. 7 shows the effect of the response function broadening in the case of the D4 diffractometer. For UO_2, only a few Bragg peaks are expected to be well resolved at forward scattering angles.

4. Experimental validation of the Monte-Carlo simulations

4.1. Validation of the coherent elastic scattering formalism

The experimental validation of our calculation scheme (Fig. 6) was performed thanks to the neutron diffraction patterns of Ruello et al. [3] measured with the D20 diffractometer by using an incident neutron energy of $E = 48.05$ meV. As shown in Fig. 1, the contribution of

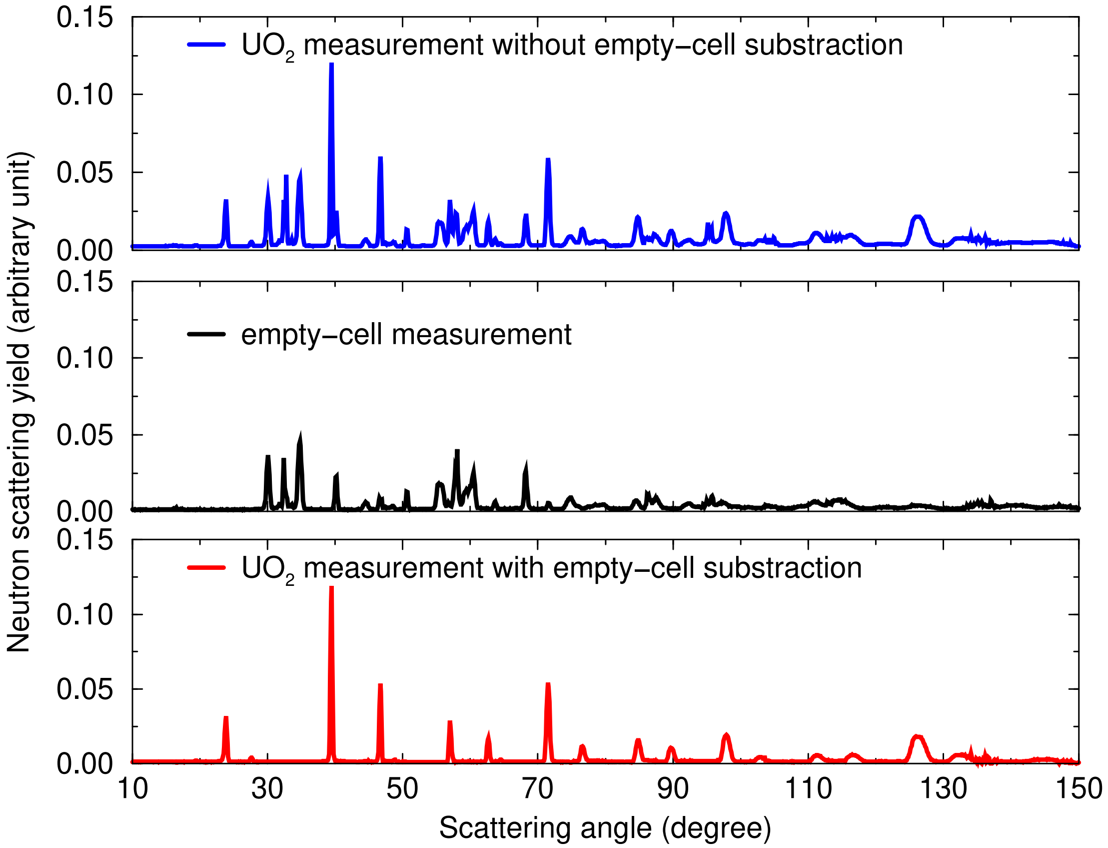

Fig. 5. Examples of neutron diffraction patterns measured on D20 at $T = 292$ K ($E = 48.05$ meV).

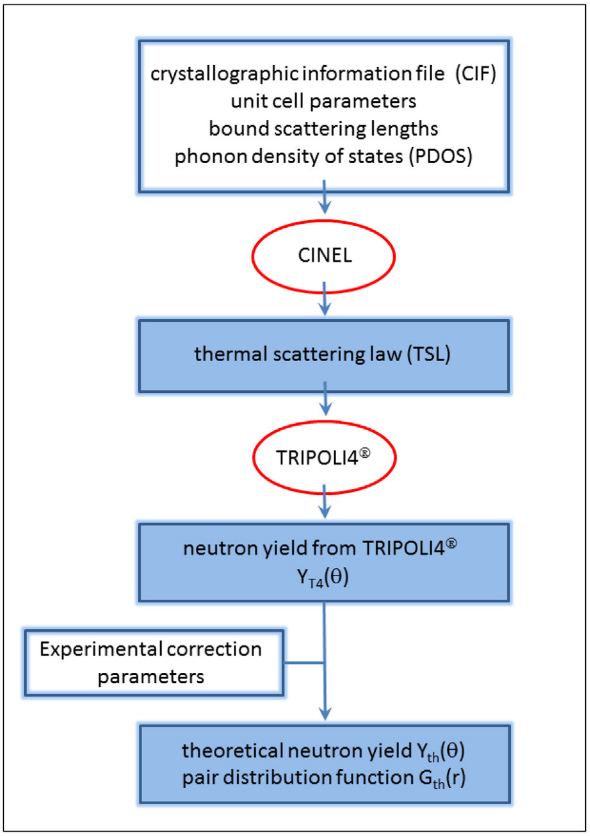

Fig. 6. Flow chart presenting the processing steps from the crystallographic information file to the theoretical neutron scattering yield and atomic pair distribution function.

the inelastic scattering cross sections around this energy is rather low. Therefore, the Ruello's data are suited to verify the implementation of the coherent elastic scattering formalism (Eq. (14)) in the CINEL processing code and its subsequent use in TRIPOLI4®.

No attempt was made to determine the UO_2 cell parameters as a function of the temperature. Such a work was already performed by Ruello [20]. His results are shown in Fig. 3. Only experimental correction parameters involved in Eqs. (16), (17) and (18) were adjusted on the experimental data by using the non-linear least-squares minimization module LMFIT [29]. The selection of the most sensitive parameters was achieved by using the Python module SALib [30]. The sensitivity analysis indicates that the constant shift C and the displacement x can be omitted from the fitting procedure. We have used $C = 0$ and $x = 0$ over the full temperature range of interest for this work.

The posterior values for the ratio y/L, the constant background C_{bkg} and U_i ($i = 1, 2, 3$) are reported in Table 2 for $T = 292$ K. The correlation matrix shows that negligible correlation coefficients exist between the angular offset, the background corrections and the response function parameters involved in the Caglioti expression. In first approximation, the experimental corrections can be assumed as independent from each other. Consequently, we decided to use the response function parameters U_i (i=1,2,3) established at 292 K for all the measured temperatures, in order to no longer smooth out possible temperature effects with the experimental broadening. The angular offset ratio y/L is a free parameter common to all the neutron diffraction patterns. Only the background correction C_{bkg} is a temperature-dependent free parameter.

The final values of the parameters are listed in Table 3. The average angular offset ratio of −0.081 is slightly lower than the values obtained at $T = 292$ K (−0.075). This trend can be explained by the displacement of the sample during the temperature rise or by a temperature-compensating bias introduced during the determination of the cell parameters. The mismatch between these two sources of

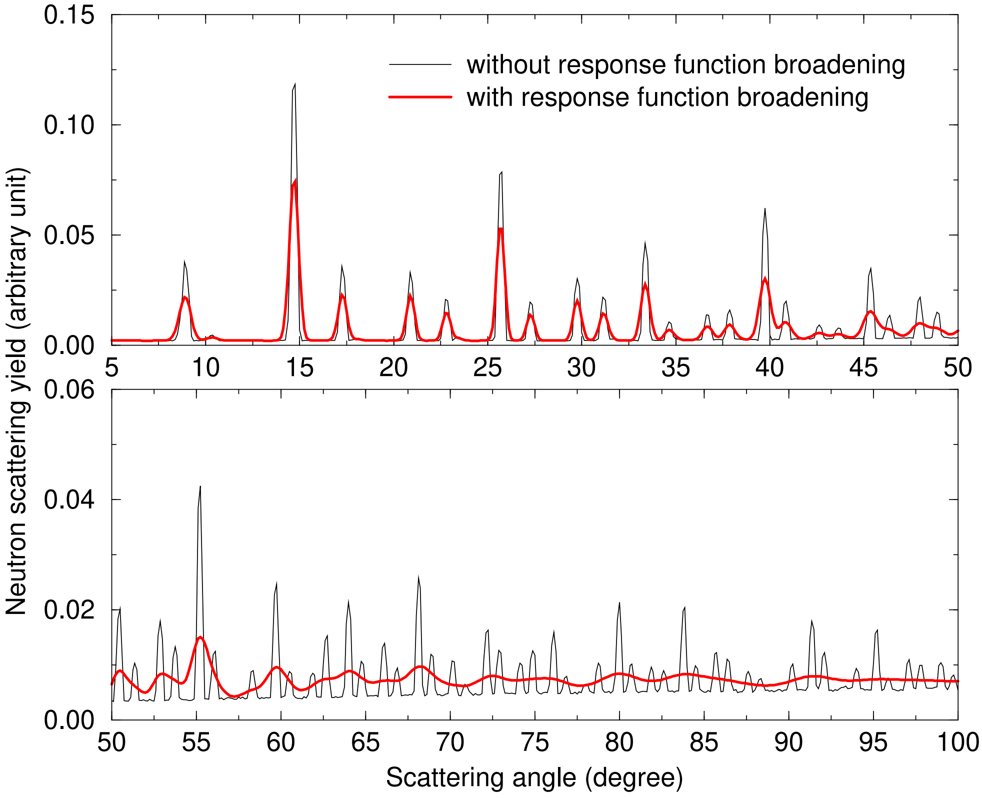

Fig. 7. Examples of theoretical neutron diffraction patterns simulated with the TRIPOLI4® code at T = 298 K for an incident neutron energy of 331.18 meV before and after broadening with the angular response function of the D4 diffractometer.

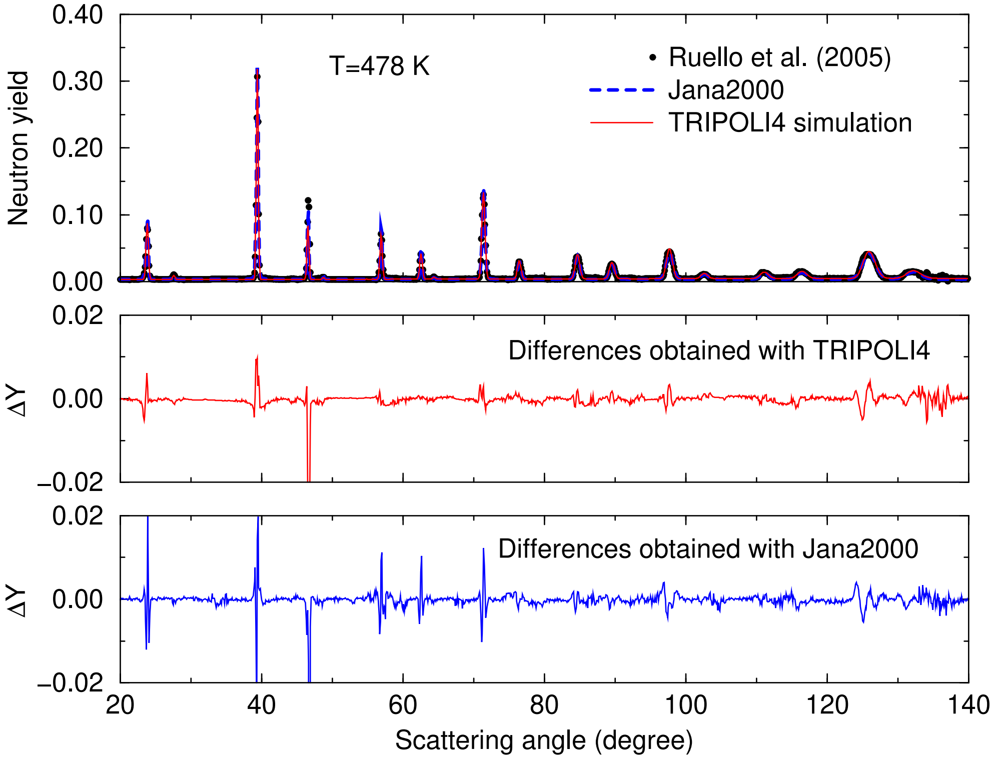

Fig. 8. Examples of theoretical results obtained with the TRIPOLI4® code and the Jana2000 refinement software [31] in the case of the UO_2 diffraction pattern measured on D20 (E = 48.05 meV) at 478 K. ΔY represents the difference between the theory and the experiment.

uncertainties as well as the sample environment which is not the same between the D4 and D20 experiments may explain the differences observed between the two sets of cell parameters shown in Fig. 3. The peak-shift obtained by Rietveld refinements is discussed in Ref. [32] through the review of discrepant cell parameters reported in the literature.

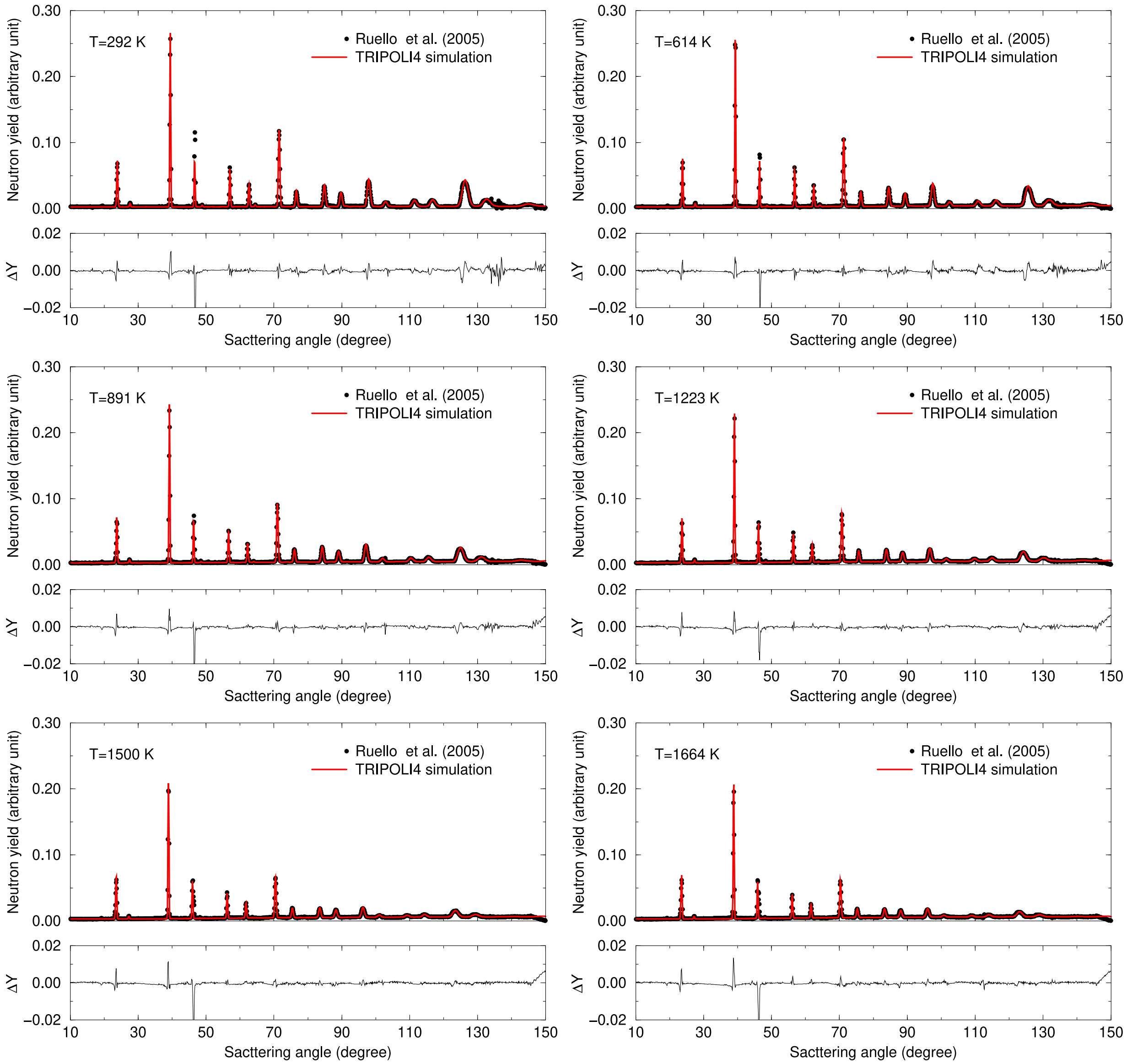

Fig. 9. Experimental and theoretical UO_2 diffraction patterns for D20 from 292 to 1664 K (E = 48.05 meV). A comparison of the results obtained at these two temperatures is shown in Fig. 10. ΔY stands for the difference between the theory and the experiment.

Table 2
Experimental correction parameters adjusted with the LMFIT module [29] on the diffraction patterns measured by Ruello et al. [3] on D20 at 292 K.

Parameters	Values	Correlation matrix				
y/L	−0.075(3)	100				
C_{bkg}	0.0024(1)	0	100			
U_1	1.49(5)	0	−14	100		
U_2	−1.01(7)	1	8	−96	100	
U_3	0.25(2)	−1	−6	91	−98	100

The result obtained at T = 478 K with our calculation scheme is compared in Fig. 8 with the diffraction pattern obtained by G. Baldinozzi [33] with the crystallographic computing system Jana2000 [31]. In both cases, the treatment of the experimental corrections relies on the same steps as presented through Eqs. (16) to (18). In the case of the Jana2000 calculations, the asymmetry of the diffraction-lines was tentatively accounted by applying the anisotropic microstrain model formulated by Stephens [34] for a cubic symmetry. The quality of each fitting procedure is illustrated by the difference $\Delta Y = Y^T_{\mathrm{th}}(\theta) - Y^T_{\mathrm{exp}}(\theta)$ between the theory and the experiment. The amplitude of the differences located at the Bragg peak positions is nearly similar between the two approaches. It highlights the difficulty to define an asymmetric response function at the forward angles which smoothly becomes symmetric with increasing scattering angles. Various solutions are reported in the literature which distinguish the diffraction optic contributions to the crystallite size and strain components.

Final calculated curves are compared to the experimental results in Fig. 9 up to 1664 K. No meaningful anomalies with increasing temperatures were observed through the behavior of ΔY as a function of the scattering angles. Nearly equivalent ΔY variations are obtained whatever the temperature is. The theoretical shape of the Bragg edges at the forward scattering angles could be improved by introducing an anisotropic diffraction-line model, as proposed in Rietveld structure refinement software. Despite such an additional correction, which is not taken into account in the present work, the closer comparison of the experimental and theoretical diffraction patterns, shown in Fig. 10, confirms that the TRIPOLI4® code is suitable for a quantitative analysis of the diffraction data by using a few numbers of free parameters. The same figure also shows that the increasing contribution of the inelastic

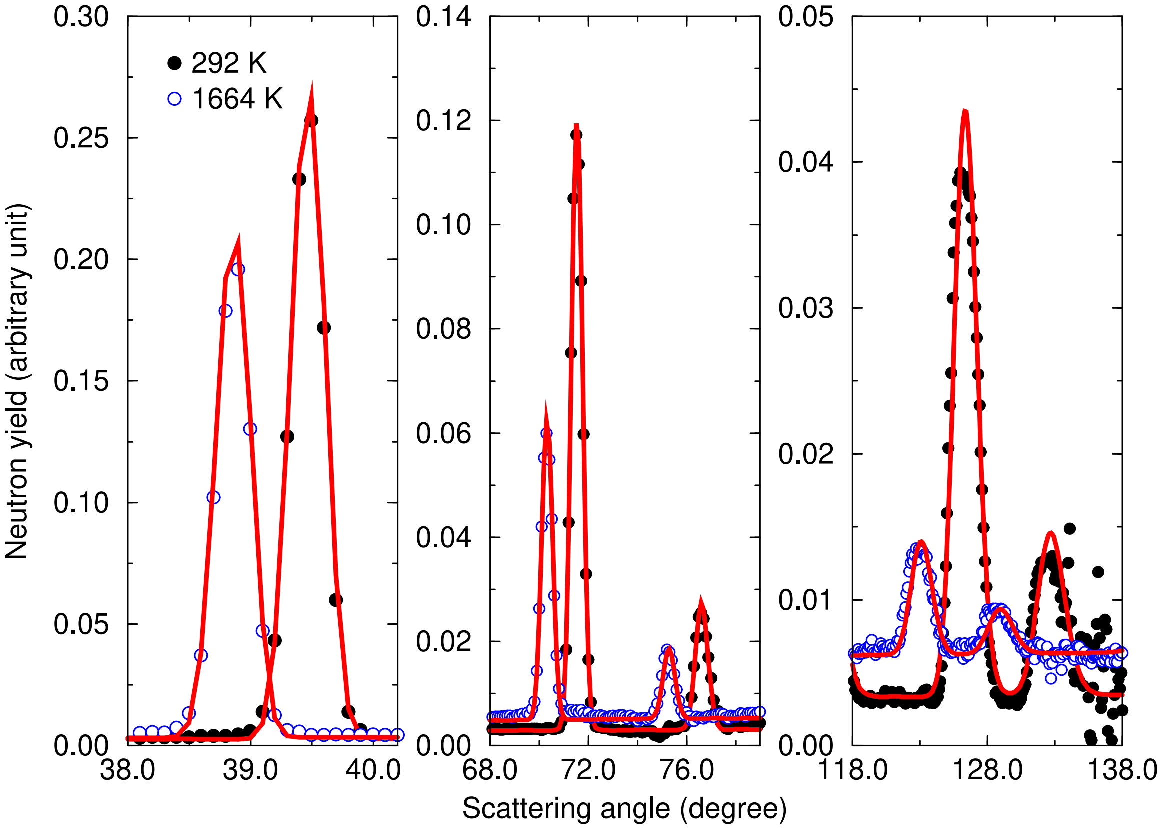

Fig. 10. Examples of experimental and theoretical UO_2 diffraction patterns (D20, $E = 48.05$ meV) obtained at 292 and 1664 K over three scattering angle ranges. The red solid lines represent the TRIPOLI4® results.

Table 3
Final values of the experimental correction parameters used in this work to describe the diffraction patterns measured by Ruello et al. [3] on D20 up to 1664 K.

Parameters	Temperatures	Values
U_1	292–1664 K	1.49(5)
U_2	292–1664 K	−1.01(7)
U_3	292–1664 K	0.25(2)
y/L	292–1664 K	−0.081(1)
C_{bkg}	292 K	0.00245(8)
C_{bkg}	478 K	0.00233(8)
C_{bkg}	614 K	0.00204(8)
C_{bkg}	752 K	0.00234(8)
C_{bkg}	891 K	0.00217(8)
C_{bkg}	1051 K	0.00214(8)
C_{bkg}	1223 K	0.00195(9)
C_{bkg}	1375 K	0.00192(8)
C_{bkg}	1500 K	0.00192(8)
C_{bkg}	1664 K	0.00172(9)

scattering with the temperature is pretty well reproduced by the Monte-Carlo calculations. However, this scattering component is rather low in the case of the D20 experiment which was performed with neutrons of energy $E = 48.05$ meV (Fig. 1). Such an issue is discussed in the next section thanks to results obtained with the D4 instrument.

4.2. Validation of the inelastic scattering formalism

The neutron diffraction patterns measured by Desgranges et al. [21] on D4 are of great interest for testing the contribution of the inelastic scattering cross sections of uranium and oxygen in UO_2 on a dense temperature grid ranging from 298 to 1273 K. Fig. 1 shows that $\sigma_j^{inel}(E)$ is no longer negligible around $E = 331.18$ meV. As shown in Fig. 11, its contribution looks like a smooth background below the Bragg edges.

The strategy used to analyze the Ruello's data was also applied to the Desgranges' data. The cell parameters introduced in the neutron cross section formalism are shown in Fig. 3. Experimental parameters whose values were optimized on the neutron diffraction patterns are listed in Table 4. The response function parameters involved in the Caglioti expression (Eq. (18)) were determined at 298 K and kept fixed up to 1273 K. The fitting procedure provided correlation coefficients between U_i ($i = 1,2,3$) as strong as those obtained for D20 (Table 2). In the case of D4, an average angular offset was determined over the full temperature range by fitting both the constant shift C and displacement x (Eq. (17)).

Fig. 12 compares the experimental and theoretical neutron diffraction patterns for D4, in which the lin-log representation highlights the increasing inelastic scattering contribution with the scattering angle. For the sake of clarity, only a few sets of temperature are shown. As already illustrated with Fig. 7, the response function of the D4 instrument makes it difficult the individual identification of the Bragg peaks above scattering angles greater than a few tens of degrees. Below $\theta = 60°$, a satisfactory agreement is achieved between the experimental and theoretical structures observed over the entire temperature range (Fig. 13).

Interesting differences between the experimental values and the theoretical curves are observed at the forward scattering angles (see green arrows in Fig. 12). They indicate that the constant background C_{bkg} introduced in Eq. (16) is not able to provide an accurate description of the data. The origin of such non-zero background correction issues as a function of the scattering angle is not well understood and needs further investigations. This result confirms that, in complement to inelastic neutron scattering instruments, the characteristics of the D4 diffractometer are suited to challenge the angular anisotropy of the neutron inelastic scattering calculated in the incoherent Gaussian approximation (Eq. (5)), whose accuracy as a function of the momentum transfer is discussed in Refs. [35,36].

Table 4
Final values of the experimental correction parameters used in this work to describe the diffraction patterns measured by Desgranges et al. [21] on D4 up to 1273 K.

Parameters	Temperatures	Values
U_1	298–1273 K	9.49(33)
U_2	298–1273 K	−3.80(19)
U_3	298–1273 K	0.53(3)
C	298–1273 K	0.106(2)
x/L	298–1273 K	0.210(4)
C_{bkg}	298 K	0.00119(3)
C_{bkg}	323 K	0.00146(3)
C_{bkg}	373 K	0.00162(3)
C_{bkg}	423 K	0.00172(4)
C_{bkg}	473 K	0.00179(4)
C_{bkg}	523 K	0.00183(4)
C_{bkg}	573 K	0.00185(4)
C_{bkg}	623 K	0.00189(4)
C_{bkg}	673 K	0.00182(4)
C_{bkg}	723 K	0.00177(4)
C_{bkg}	773 K	0.00174(4)
C_{bkg}	823 K	0.00170(5)
C_{bkg}	873 K	0.00171(5)
C_{bkg}	973 K	0.00161(5)
C_{bkg}	1023 K	0.00158(5)
C_{bkg}	1073 K	0.00149(5)
C_{bkg}	1123 K	0.00150(5)
C_{bkg}	1173 K	0.00145(5)
C_{bkg}	1223 K	0.00144(6)
C_{bkg}	1273 K	0.00128(6)

4.3. From neutron diffraction patterns to atomic pair distributions

The experimental program carried out on the D4 diffractometer was originally designed to investigate the validity of the Fm$\bar{3}$m symmetry as a function of the temperature. Deviations from the average structure of UO_2 have been analyzed via atomic pair distribution functions $G(r)$, which give the probability of finding an atom at a distance r from a given atom. The expression of $G(r)$ depends on the total scattering structure factor $S(Q)$:

$$G(r) = \frac{2}{\pi} \int_{Q_{\min}}^{Q_{\max}} Q(S(Q) - 1) \sin(Qr) dQ. \tag{19}$$

For neutron diffraction experiments, $S_{\text{exp}}(Q)$ is defined as follow:

$$S_{\text{exp}}(Q) = \frac{Y^T_{\text{exp}}(Q)\,(1 - \mathcal{P}(Q)) - \sum_{j=1}^{N} c_j |b_j|^2}{|\sum_{j=1}^{N} c_j b_j|^2} + 1, \tag{20}$$

where $c_j = 1/N$ and b_j represent the concentration and the bound scattering length of the jth nucleus in the unit cell of the studied material. The inelasticity correction $1 - \mathcal{P}(Q)$ was taken from the work of Desgranges, in which a Placzek-type analytical correction [37] was applied to the normalized experimental neutron scattering yields. The proposed correction is well appropriate to the D4 experiment that involves heavy atoms and an incident neutron energy of E = 331.18 meV. These conditions allow to assume that the average amount of energy exchanged with the scattering system is small compared to the excitation energies of that system.

The experimental and theoretical atomic pair distribution functions for UO_2 are compared in Fig. 14 from room temperature to 1273 K. The Monte-Carlo simulations were performed by using the Fm$\bar{3}$m group space with harmonic atomic vibrations. The first three peaks mainly correspond to the U–O, O–O and U–U bonds [38]. A closer inspection of the experimental results indicates a negative peak-shift of −0.010(5) Å for the U–O bond from 298 K to 1273 K, while the peak position of the U–U bond increases by +0.020(5) Å. By contrast, the Monte-Carlo simulations provide positive peak-shifts which are close to +0.040(5) Å for both U–O and U–U bonds.

Table 5
Oxygen site occupancy in the UO_2 unit cell in the case of the ideal fluorite structure and four-site model.

Ideal fluorite structure			Four-site model		
x	y	z	x	y	z
1/4	1/4	1/4	$1/4+\delta$	$1/4+\delta$	$1/4+\delta$
			$1/4+\delta$	$1/4-\delta$	$1/4-\delta$
			$1/4-\delta$	$1/4+\delta$	$1/4-\delta$
			$1/4-\delta$	$1/4-\delta$	$1/4+\delta$
1/4	3/4	3/4	$1/4+\delta$	$3/4+\delta$	$3/4+\delta$
			$1/4+\delta$	$3/4-\delta$	$3/4-\delta$
			$1/4-\delta$	$3/4+\delta$	$3/4-\delta$
			$1/4-\delta$	$3/4-\delta$	$3/4+\delta$
3/4	1/4	3/4	$3/4+\delta$	$1/4+\delta$	$3/4+\delta$
			$3/4+\delta$	$1/4-\delta$	$3/4-\delta$
			$3/4-\delta$	$1/4+\delta$	$3/4-\delta$
			$3/4-\delta$	$1/4-\delta$	$3/4+\delta$
3/4	3/4	1/4	$3/4+\delta$	$3/4+\delta$	$1/4+\delta$
			$3/4+\delta$	$3/4-\delta$	$1/4-\delta$
			$3/4-\delta$	$3/4+\delta$	$1/4-\delta$
			$3/4-\delta$	$3/4-\delta$	$1/4+\delta$
3/4	3/4	3/4	$3/4-\delta$	$3/4-\delta$	$3/4-\delta$
			$3/4-\delta$	$3/4+\delta$	$3/4+\delta$
			$3/4+\delta$	$3/4-\delta$	$3/4+\delta$
			$3/4+\delta$	$3/4+\delta$	$3/4-\delta$
3/4	1/4	1/4	$3/4-\delta$	$1/4-\delta$	$1/4-\delta$
			$3/4-\delta$	$1/4+\delta$	$1/4+\delta$
			$3/4+\delta$	$1/4-\delta$	$1/4+\delta$
			$3/4+\delta$	$1/4+\delta$	$1/4-\delta$
1/4	3/4	1/4	$1/4-\delta$	$3/4-\delta$	$1/4-\delta$
			$1/4-\delta$	$3/4+\delta$	$1/4+\delta$
			$1/4+\delta$	$3/4-\delta$	$1/4+\delta$
			$1/4+\delta$	$3/4+\delta$	$1/4-\delta$
1/4	1/4	3/4	$1/4-\delta$	$1/4-\delta$	$3/4-\delta$
			$1/4-\delta$	$1/4+\delta$	$3/4+\delta$
			$1/4+\delta$	$1/4-\delta$	$3/4+\delta$
			$1/4+\delta$	$1/4+\delta$	$3/4-\delta$

Our calculations agree with past works reported in the literature. They all conclude that the arrangement of the uranium and oxygen atoms cannot be described in term of an ideal fluorite structure at elevated temperature. The observed differences between the experiment and the theory correspond to an unexpected shortening of the U–O distance with increasing temperature. The underlying mechanism is not well understood. It is the subject of debates in the literature. Willis interprets the temperature effects on the lattice arrangement in terms of anharmonic atomic vibrations [2,39,40]. Similarly, Skinner et al. [41] favor atomic disorder mechanisms in the Fm$\bar{3}$m group space for explaining the U–O and U–U bond lengths deduced from X-ray diffraction patterns measured up to the UO_2 melting point. By contrast, the existence of a local symmetry (such as Pa$\bar{3}$) is suggested by Desgranges et al. [21] for explaining the shortening of the U–O distance at 1273 K (Fig. 14). These different approaches are discussed in the next section.

5. Perspectives for improving the CINEL calculations

5.1. Investigation of a four-site model for the oxygen atoms

On the basis of single-crystal neutron diffraction data on UO_2 measured from 293 to 1373 K, Willis notices that a better agreement between the calculated and the experimental data is obtained by relaxing the oxygen atoms from their regular positions in the ideal fluorite structure [2]. In this model, the uranium atoms remain in the same positions (0, 0, 0), (0, 1/2, 1/2), (1/2, 0, 1/2) and (1/2, 1/2, 0), while every single oxygen atom is split into four 1/4 atom and they are located in the (111) directions toward the four neighbored interstices with a relaxation term δ. Detailed positions of the oxygen atoms in the four-site model are presented in Table 5.

As all the coordinates of the atom position are known, the form factor given by Eq. (15) can be explicitly expressed for the four-site model as follow:

$$F_{4s}(\vec{\tau}_{hkl}) = \begin{cases} 4b_U \exp\left(-\frac{\hbar^2\tau^2_{hkl}}{4M_Uk_BT}\Lambda_U(T)\right) + 8b_O \exp\left(-\frac{\hbar^2\tau^2_{hkl}}{4M_Ok_BT}\Lambda_O(T)\right) f_1 \\ \quad \text{if } h+k+l = 4n \text{ and } h,\ k,\ l \text{ all even} \\ 4b_U \exp\left(-\frac{\hbar^2\tau^2_{hkl}}{4M_Uk_BT}\Lambda_U(T)\right) + 8b_O \exp\left(-\frac{\hbar^2\tau^2_{hkl}}{4M_Ok_BT}\Lambda_O(T)\right) f_2 \\ \quad \text{if } h+k+l = 4n+1 \text{ and } h,\ k,\ l \text{ all odd} \\ 4b_U \exp\left(-\frac{\hbar^2\tau^2_{hkl}}{4M_Uk_BT}\Lambda_U(T)\right) - 8b_O \exp\left(-\frac{\hbar^2\tau^2_{hkl}}{4M_Ok_BT}\Lambda_O(T)\right) f_1 \\ \quad \text{if } h+k+l = 4n+2 \text{ and } h,\ k,\ l \text{ all even} \\ 4b_U \exp\left(-\frac{\hbar^2\tau^2_{hkl}}{4M_Uk_BT}\Lambda_U(T)\right) - 8b_O \exp\left(-\frac{\hbar^2\tau^2_{hkl}}{4M_Ok_BT}\Lambda_O(T)\right) f_2 \\ \quad \text{if } h+k+l = 4n+3 \text{ and } h,\ k,\ l \text{ all odd} \\ 0 \quad \text{otherwise} \end{cases} \tag{21}$$

in which $f_1 = \cos(2\pi\delta h)\cos(2\pi\delta k)\cos(2\pi\delta l)$ and $f_2 = \sin(2\pi\delta h)\sin(2\pi\delta k)\sin(2\pi\delta l)$. Willis proposed to rewrite Eq. (21) in the following compact form:

$$F_{4s}(\vec{\tau}_{hkl}) = \begin{cases} 4b_U \exp\left(-\frac{\hbar^2\tau^2_{hkl}}{4M_Uk_BT}\Lambda_U(T)\right) \\ \quad + 8b_O \exp\left(-\frac{\hbar^2\tau^2_{hkl}}{4M_Ok_BT}\Lambda_O(T)\right) f_{4s} \\ \quad \text{if } h,\ k,\ l \text{ all odd or all even} \\ 0 \quad \text{otherwise} \end{cases} \tag{22}$$

with

$$f_{4s} = \cos\left(2\pi h\left(\frac{1}{4}+\delta\right)\right)\cos\left(2\pi k\left(\frac{1}{4}+\delta\right)\right)\cos\left(2\pi l\left(\frac{1}{4}+\delta\right)\right). \tag{23}$$

The implementation of the four-site model in the CINEL code leads to the theoretical results shown in Fig. 15a, which were obtained in the case of the D4 experiment for T =1273 K with a relaxation term $\delta = 0.0177$ given in Ref. [21]. Compared to the ideal fluorite structure, no improvement is observed at elevated temperature when the four-site model is introduced in the fitting procedure. The differences with the experimental values increase with the hkl values in the scattering angle range shown in Fig. 15a.

In the case of an ideal fluorite structure ($\delta = 0$), Eq. (21) shows that the intensity of the form factor for $h+k+l = 4n$ is more important than that of $h+k+l = 4n\pm1$ and $h+k+l = 4n+2$, because in such a case the uranium and oxygen atoms scatter in-phase. For $h+k+l = 4n+2$, the intensity of the form factor is weak because they scatter out-of-phase. For $h+k+l = 4n\pm1$, the intensity is medium since only the uranium atoms contribute to the scattering. The introduction of the relaxation term $\delta \neq 0$ not only weaken the strongest in-phase scattering, but also strengthen the weakest out-of-phase scattering. Such an effect increases with the hkl values until its peak value, and decreases for large hkl values because of the dominance of the exponential term in Eq. (22) which involves $-\tau^2_{hkl}$. As a consequence, the four-site model proposed by Willis is not an adequate solution to introduce an oxygen disorder mechanism in the CINEL model.

5.2. Investigations of a non-zero anharmonic third-cumulant coefficient for the oxygen atoms

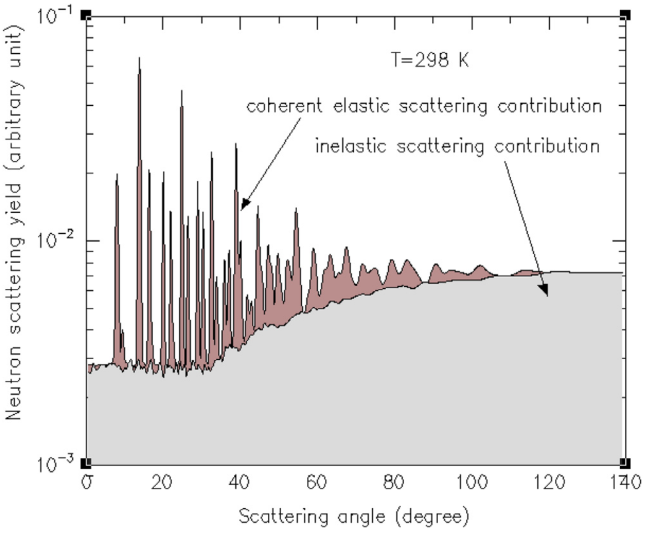

Fig. 11. Inelastic and coherent elastic scattering contributions simulated with the TRIPOLI4® code at T = 298 K for D4 (E = 331.18 meV).

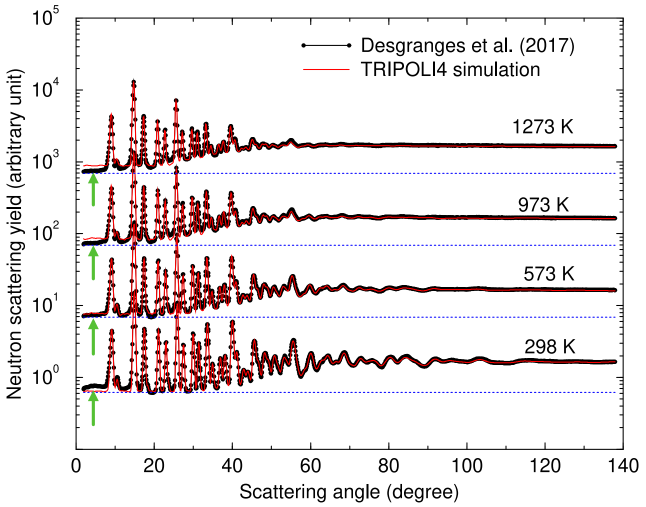

Fig. 12. Experimental and theoretical UO_2 diffraction patterns for D4 from 298 to 1273 K (E = 331.18 meV). A comparison of the results obtained at these two temperatures is shown in Fig. ??. The green arrows highlight the differences observed between the experiment and the theory at the forward scattering angles. The dotted blue lines show the increasing inelastic scattering contribution with the scattering angle.

In order to favor anharmonic oxygen vibrations in the fluorite structure instead of a disorder mechanism only based on the displacement of the oxygen atoms from their equilibrium positions, Willis and Hazell [40] re-analyzed the single-crystal diffraction data on UO_2 (Section 5.1) by introducing third-cumulant coefficients in the form factor $F(\vec{\tau}_{hkl})$ (Eq. (15)). In theory, there are up to ten third-cumulant coefficients for each atom j. However, Willis and Hazell concluded that only the third-cumulant coefficient of the oxygen atoms c^{O}_{123} is non-vanishing when using the symmetry properties of the ideal fluorite structure. According to their work, the anharmonic form factor becomes:

$$F_{\text{anhar}}(\vec{\tau}_{hkl}) = \sum_{j=1}^{N} b_j \exp\left(-\frac{\hbar^2\tau^2_{hkl}}{4M_jk_BT}\Lambda_j(T)\right) \times \exp\left(i\vec{\tau}_{hkl}\cdot\vec{p}_j - i\delta_{jO}c^{O}_{123}\tau^3_{hkl}\right), \tag{24}$$

where δ_{jO} is the Kronecker delta function which is equal to 1 if atom j is oxygen and 0 for uranium. By analogy with Eq (22), $F_{\text{anhar}}(\vec{\tau}_{hkl})$ can

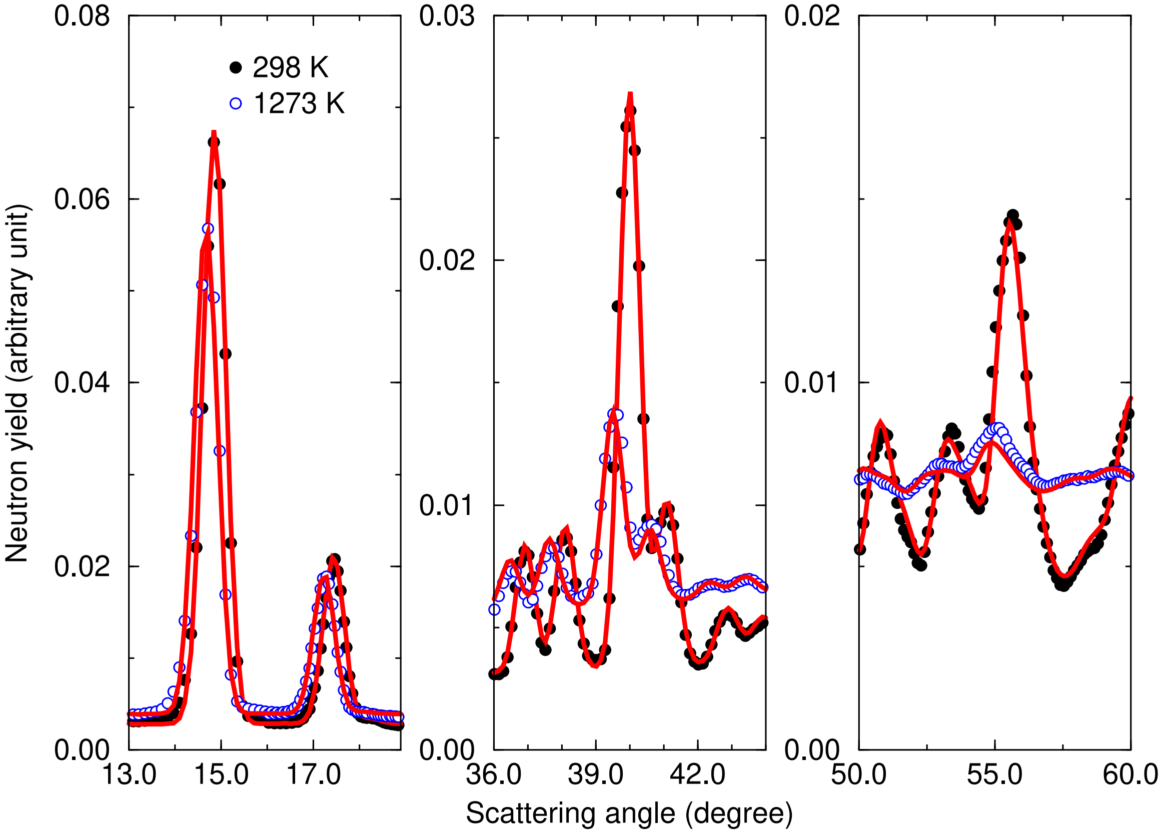

Fig. 13. Examples of experimental and theoretical UO_2 diffraction patterns (D4, $E = 331.18$ meV) obtained at 298 and 1273 K over three scattering angle ranges. The red solid lines represent the TRIPOLI4® results.

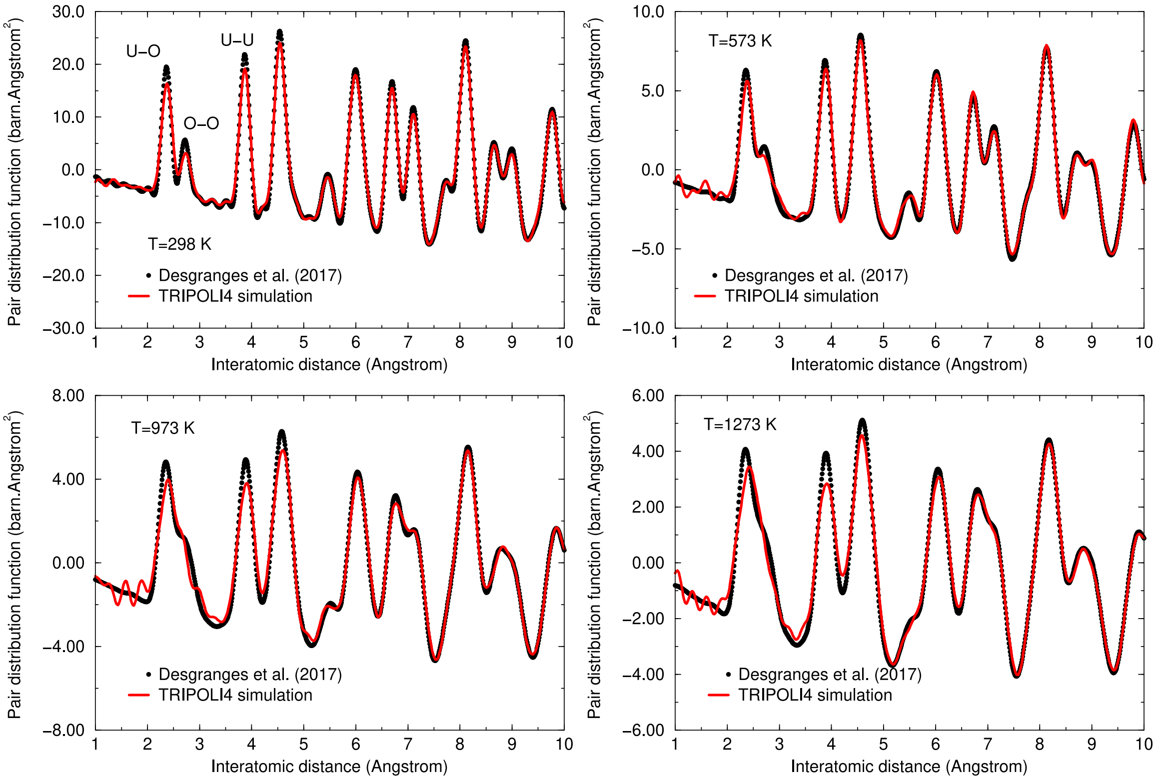

Fig. 14. Experimental and theoretical atomic pair distribution functions for UO_2 (D4, $E = 331.18$ meV). The TRIPOLI4® simulation were performed by using the $Fm\bar{3}m$ space group with harmonic atomic vibrations. The first three peaks mainly corresponds to the U–O, O–O and U–U bonds [38].

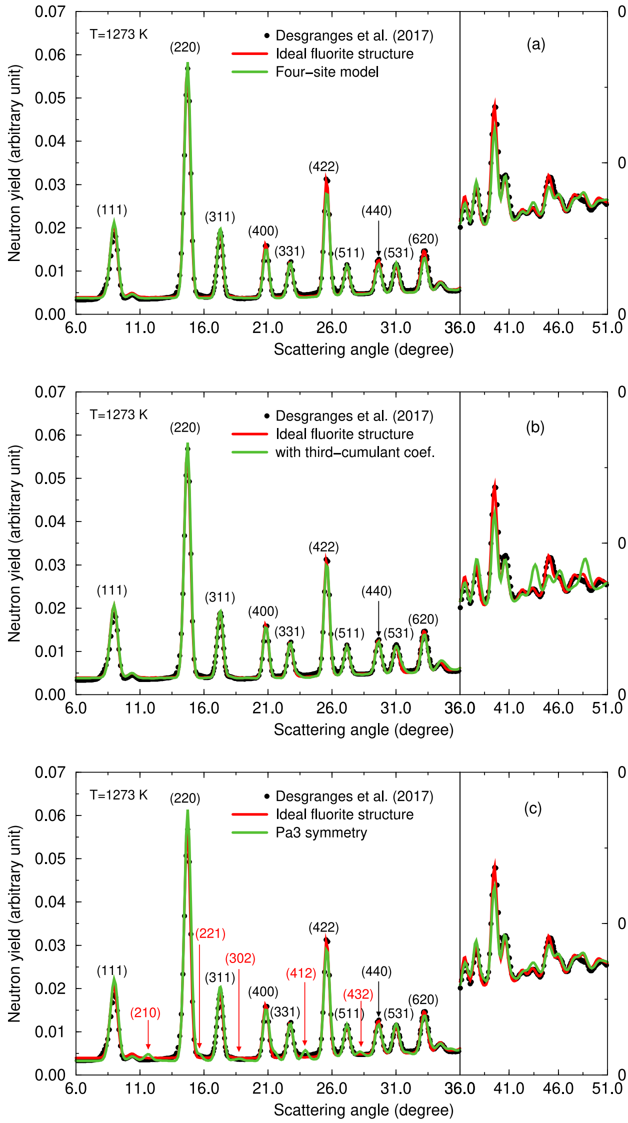

Fig. 15. The experimental diffraction patterns measured on D4 at T =1273 K (E = 331.18 meV) and theoretical results obtained with the ideal fluorite structure are compared to results obtained with (a) a four-site model for the oxygen atoms with a relaxation term $\delta = 0.0177$, (b) a structure factor equation with a non-zero anharmonic third-cumulant coefficient for the oxygen atoms ($c^{\mathrm{O}}_{123} = 0.0017$ and (c) a Pa$\bar{3}$ symmetry with the same relaxation term as in the four-site model ($\delta = 0.0177$). The (hkl) plans for the fluorite structure are indicated in black for the well resolved peaks observed below $\theta = 36°$. The additional (hkl) peaks due to the $Pa\bar{3}$ symmetry are indicated in red.

Table 6
Oxygen site occupancy in the UO$_2$ unit cell in the case of the Fm$\bar{3}$m and Pa$\bar{3}$ symmetries.

Fm$\bar{3}$m symmetry			Pa$\bar{3}$ symmetry		
x	y	z	x	y	z
1/4	1/4	1/4	$1/4+\delta$	$1/4+\delta$	$1/4+\delta$
1/4	3/4	3/4	$1/4-\delta$	$3/4-\delta$	$3/4+\delta$
3/4	1/4	3/4	$3/4+\delta$	$1/4-\delta$	$3/4-\delta$
3/4	3/4	1/4	$3/4-\delta$	$3/4+\delta$	$1/4-\delta$
3/4	3/4	3/4	$3/4-\delta$	$3/4-\delta$	$3/4-\delta$
3/4	1/4	1/4	$3/4+\delta$	$1/4+\delta$	$1/4-\delta$
1/4	3/4	1/4	$1/4-\delta$	$3/4+\delta$	$1/4+\delta$
1/4	1/4	3/4	$1/4+\delta$	$1/4-\delta$	$3/4+\delta$

be rewritten as

$$F_{\mathrm{anhar}}(\vec{\tau}_{hkl}) = \begin{cases} 4b_U \exp\left(-\dfrac{\hbar^2\tau^2_{hkl}}{4M_U k_B T}\Lambda_U(T)\right) \\ \quad +8b_O \exp\left(-\dfrac{\hbar^2\tau^2_{hkl}}{4M_O k_B T}\Lambda_O(T)\right) f_{\mathrm{anhar}} \\ \quad\text{if } h,\ k,\ l \text{ all odd or all even} \\ 0 \quad \text{otherwise.} \end{cases} \tag{25}$$

with

$$f_{\mathrm{anhar}} = \exp\left(-ic^{\mathrm{O}}_{123}\tau^3_{hkl}\right)\cos\left(\pi\frac{h}{2}\right)\cos\left(\pi\frac{k}{2}\right)\cos\left(\pi\frac{l}{2}\right). \tag{26}$$

For (hkl) peaks satisfying $h+k+l = 4n \pm 1$, anharmonicity vanishes ($f_{\mathrm{anhar}} = 0$) when uranium atoms contribute to the scattering. For (hkl) peaks satisfying $h+k+l = 4n$ or $h+k+l = 4n+2$, $f_{\mathrm{anhar}} = \pm\exp(-ic^{\mathrm{O}}_{123}\tau^3_{hkl})$ and $|F_{\mathrm{anhar}}(\vec{\tau}_{hkl})|^2$ is given by:

$$|F_{\mathrm{anhar}}(\vec{\tau}_{hkl})|^2 = |F(\vec{\tau}_{hkl})|^2 \mp 128 b_U b_O \times \exp\left(-\frac{\hbar^2\tau^2_{hkl}}{4k_B T}\left(\frac{\Lambda_U(T)}{M_U} + \frac{\Lambda_O(T)}{M_O}\right)\right)\sin^2\left(\frac{c^{\mathrm{O}}_{123}\tau^3_{hkl}}{2}\right), \tag{27}$$

in which $|F(\vec{\tau}_{hkl})|^2$ represents the square of the form factor in the case of an ideal fluorite structure.

Fig. 15b shows the theoretical results calculated at $T = 1273$ K in the case of the D4 experiment with an anharmonic third-cumulant coefficient c^{O}_{123} equal to 0.0017. This value was obtained from the interpolation of the results reported in Ref. [40]. The agreement with the experiment is not improved by using $c^{\mathrm{O}}_{123} \neq 0$. On the contrary, significant differences are observed for scattering angles greater than 40°. According to Eq. (27), the intensity of the strongest U–O in-phase scattering will be weakened, while the weakest out-of-phase scattering will be strengthened. The present result indicates that the term $c^{\mathrm{O}}_{123}\tau^3_{hkl}$ in Eq. (27) is not able to simulate the anharmonic behavior of the oxygen atoms in our calculation scheme at elevated temperatures.

5.3. Investigations of the Pa$\bar{3}$ symmetry

The experimental results measured on the D4 instrument have been originally analyzed by Desgranges et al. [21]. They investigated the possibility of using the Pa$\bar{3}$ crystalline symmetry as a local configuration in UO$_2$, instead of the ideal fluorite structure, for explaining the shortening of the U–O distance with increasing temperature. In this section, we show how the theoretical diffraction patterns change when the Pa$\bar{3}$ symmetry is used as an average configuration for UO$_2$.

Compared to the ideal fluorite structure, the positions of the uranium atoms in the Pa$\bar{3}$ symmetry remain the same while those of oxygen are modified with a relaxation term δ (Table 6). The oxygen cage is thus distorted to form two long U–O distances and six short U–O distances. Such an oxygen site occupancy can be regarded as a specific configuration of the four-site model (Table 5). Desgranges et al. show that the first few peaks observed in the pair distribution function of UO$_2$ at 1273 K (Fig. 14) are better reproduced by distinguishing these two U–O distances.

The theoretical diffraction pattern calculated at 1273 K in the case of the D4 experiment under the assumption of the Pa$\bar{3}$ symmetry is reported in Fig. 15c. The differences between the experiment and the theory are nearly of the same order of magnitude than those obtained with the four-site model. The main problem compared to the ideal fluorite structure is the presence of new (hkl) peaks in the theoretical diffraction pattern which are not observed in the experimental one. According to Eq. (21), the Bragg diffractions in the ideal fluorite structure occur for (hkl) plan when h, k, l are all odd or all even. The distortion of the oxygen cage in the Pa$\bar{3}$ symmetry allows Bragg diffractions in (hkl) plan even if h, k, l are not all odd and not all even. In response to this drawback, outgoing experimental and theoretical works are in progress for exploring other alternative symmetries that will satisfy the average and local structures of UO$_2$ at elevated temperatures.

6. Conclusions

The results reported in this paper indicate that the Monte-Carlo neutron transport code TRIPOLI4® is able to reproduce neutron diffraction patterns measured at ILL up to 1664 K thanks to the newly developed processing tool CINEL. The neutron cross section formalism implemented in CINEL allows to calculate the inelastic and coherent elastic scattering contributions by using an ideal fluorite structure for UO_2 over the full temperature range. A few numbers of experimental parameters were optimized on the data to account for the angular offset, the response function of the diffractometer and a background correction. The good agreement between the experimental and theoretical neutron diffraction patterns validates our TRIPOLI4® calculation scheme for UO_2. However some limited issues remain in the interpretation of the background correction. Biases due to theoretical approximations would need to be investigated.

The performance of our calculation scheme was also investigated by simulating atomic pair distribution functions to probe the structure of UO_2 at elevated temperature. The differences observed at 1273 K between the experiment and the theory confirm that the local deviations of the oxygen atoms from the average structure of UO_2 are not compatible with an ideal fluorite structure. We show that the CINEL processing tool offers the possibility of testing atomic disorder configurations, anharmonic models or space groups which are suggested in the literature for exploring the unexpected shortening of the U–O distance with increasing temperature.

The neutron cross sections for UO_2, calculated with the processing tool CINEL, will be delivered at the JEFF project of the OECD/NEA databank. Formatting options allow to automatically produce thermal scattering law files with respect to the nuclear data format requirements.

CRediT authorship contribution statement

S. Xu: Conceptualization, Methodology, Software, Writing - original draft. **G. Noguere:** Conceptualization, Methodology, Software, Writing - review & editing. **L. Desgranges:** Investigation, Resources. **J.I. Marquez Damian:** Methodology, Resources.

Declaration of competing interest

The authors declare that they have no known competing financial interests or personal relationships that could have appeared to influence the work reported in this paper.

Acknowledgments

The authors wish to express their appreciations for the experimental work performed at ILL with the support of H.E. Fisher and T. Hansen. A special thanks goes to G. Baldinozzi, from CNRS Centrale Supelec, for the results obtained with the Jana2000 software. We express our gratitude to them for sharing the data used in this work.

References

[1] B.T.M. Willis, Proc. R. Soc. Lond. A 274 (1963) 122.
[2] B.T.M. Willis, Proc. R. Soc. Lond. A 274 (1963) 134.
[3] P. Ruello, et al., J. Phys. Chem. Solids 66 (2005) 823.
[4] Y. Ma, A Study of Point Defects in UO_{2+x} and their Impact Upon Fuel Properties (Ph.D. thesis), Aix-Marseille University, 2017.
[5] E. Brun, et al., Ann. Nucl. Energy 82 (2015) 151.
[6] H.M. Rietveld, J. Appl. Crystallogr. 2 (1969) 65.
[7] V.F. Sears, Neut. News 3 (1992) 26.
[8] R.E. MacFarlane, A.C. Kahler, Nucl. Data Sheets 111 (2010) 2739.
[9] Y. Zhu, A.I. Hawari, Full Law Analysis Scattering System Hub (FLASSH), in: Proc. Int. Conf. PHYSOR 2018, Cancun, Mexico, 2018.
[10] T. Kittelmann, M. Boin, Comput. Phys. Comm. 189 (2015) 114.
[11] K. Hartling, et al., Nucl. Instrum. Methods A 891 (2018) 25.
[12] https://www.ncnr.nist.gov/resources/n-lengths/elements/u.html.
[13] A.M. Lane, R.G. Thomas, Rev. Modern Phys. 30 (1958) 257.
[14] G. Noguere, P. Maldonado, C. De Saint Jean, Eur. Phys. J. Plus 133 (2018) 177.
[15] G. Noguere, et al., Phys. Rev. B 102 (2020) 134312.
[16] L. Van Hove, Phys. Rev. 95 (1954) 249.
[17] A.W. Solbrig, Amer. J. Phys. 29 (1961) 257.
[18] A. Sjolander, Arkiv Fysik 14 (1958) 315.
[19] G.L. Squires, Proc. R. Soc. A 212 (1952) 192.
[20] P. Ruello, Etude du changement de comportement du dioxyde d'uranium au voisinage de 1300 K (Ph.D. thesis), Ecole Centrale Paris, 2001.
[21] L. Desgranges, et al., Inorg. Chem. 56 (2017) 321.
[22] X.X. Cai, T. Kittelmann, Comput. Phys. Comm. 246 (2020) 106851.
[23] https://materialsproject.org/materials/mp-1597.
[24] https://www.ill.eu/users/instruments/instruments-list/.
[25] H.E. Fischer, et al., Appl. Phys. A 74 (2002) 160.
[26] A. Trkov, D.A. Brown, ENDF-6 Format Manual, Technical Report BNL-203218-2018-INRE, Brookhaven National Laboratory, 2018.
[27] L.B. McCusker, et al., J. Appl. Crystallogr. 32 (1999) 36.
[28] G. Caglioti, et al., Nucl. Instrum. 3 (1958) 223.
[29] M. Newville, et al., Lmfit/lmfit-py 1.0.1, 2020.
[30] J. Herman, W. Usher, J. Open Source Soft. 2 (2017) 97.
[31] V. Petricek, M. Dusek, L. Palatinus, Z. Kristallogr. 229 (5) (2014) 345.
[32] M. Tsubota, et al., Results Phys. 15 (2019) 102640.
[33] G. Baldinozzi, Private communication, 2021.
[34] P. Stephens, J. Appl. Crystallogr. 32 (1999) 281.
[35] B.R.A. Nijboer, A. Rahman, Physica 32 (1966) 415.
[36] H. Schober, J. Neut. Res. 17 (2014) 109.
[37] G. Placzek, Phys. Rev. 86 (1952) 377.
[38] R.I. Palomares, et al., Phys. Rev. B 3 (2019) 053611.
[39] B.T.M. Willis, J. Phys. 25 (1964) 431.
[40] B.T.M. Willis, R.G. Hazell, Acta Crystallogr. 36 (1980) 582.
[41] L.B. Skinner, et al., Science 346 (2014) 984.